Hydrology and Earth System Sciences Discussions

Optimisation of LiDAR derived terrain models for river flow modelling

G. Mandlburger[1], C. Hauer[2], B. Höfle[3], H. Habersack[2], and N. Pfeifer[3]

[1]Christian Doppler Laboratory "Spatial Data from Laser Scanning and Remote Sensing" at the Institute of Photogrammetry and Remote Sensing, Vienna University of Technology, Gusshausstrasse 27–29, 1040 Vienna, Austria
[2]Institute of Water Management, Hydrology and Hydraulic Engineering, BOKU – University of Applied Life Sciences, Muthgasse 107, 1190 Vienna, Austria
[3]Institute of Photogrammetry and Remote Sensing, Vienna University of Technology, Gusshausstrasse 27–29, 1040 Vienna, Austria

HESSD

5, 3605–3638, 2008

Optimisation of LiDAR DTMs for river flow modelling

G. Mandlburger et al.

Title Page	
Abstract	Introduction
Conclusions	References
Tables	Figures
◄◄	►►
◄	►
Back	Close
Full Screen / Esc	
Printer-friendly Version	
Interactive Discussion	

Optimisation of LiDAR DTMs for river flow modelling

G. Mandlburger et al.

Abstract

Airborne LiDAR (Light Detection And Ranging) combines cost efficiency, high degree of automation, high point density of typically 1–10 points per m^2 and height accuracy of better than ±15 cm. For all these reasons LiDAR is particularly suitable for deriving
5 precise Digital Terrain Models (DTM) as geometric basis for hydrodynamic-numerical (HN) simulations. The application of LiDAR for river flow modelling requires a series of preprocessing steps. Terrain points have to be filtered and merged with river bed data, e.g. from echo sounding. Then, a smooth Digital Terrain Model of the Watercourse (DTM-W) needs to be derived, preferably considering the random measurement error
10 during surface interpolation. In a subsequent step, a hydraulic computation mesh has to be constructed. Hydraulic simulation software is often restricted to a limited number of nodes and elements, thus, data reduction and data conditioning of the high resolution LiDAR DTM-W becomes necessary. We will present a DTM thinning approach based on adaptive TIN refinement which allows a very effective compression of the point
15 data (more than 95% in flood plains and up to 90% in steep areas) while preserving the most relevant topographic features (height tolerance ±20 cm). Traditional hydraulic mesh generators focus primarily on physical aspects of the computation grid like aspect ratio, expansion ratio and angle criterion. They often neglect the detailed shape of the topography as provided by LiDAR data. In contrast, our approach considers both the
20 high geometric resolution of the LiDAR data and additional mesh quality parameters. It will be shown that the modelling results (flood extents, flow velocities, etc.) can vary remarkably by the availability of surface details. Thus, the inclusion of such geometric details in the hydraulic computation meshes will gain importance for river flow modelling in the future.

1 Introduction

Hydrodynamic-numerical (HN) modelling – also referred to as Computational Fluid Dynamic (CFD) modelling – is widespread in water sciences. Simulation tools are used for ecological studies (Hauer et al., 2008a,b) as well as for all kinds of hydraulic engineering purposes such as river restoration and the like (Denoth, 2003; Gouda et al., 2002; Khan and Barkdoll, 2000; Fischer-Antze et al., 2001). Moreover, the precise delineation of endangered or vulnerable areas in flood hazard analysis is also based on hydrodynamic-numerical models (Habersack and Gaul, 2008). In many countries, land use regulations and building codes are directly linked to flood hazard maps, which show areas affected by events with a certain return period.

In the UK, France, United States, Canada, and New Zealand, the area affected by a 100-year flood (HQ100) plays an essential role for flood mitigation (Marco, 1994; Watt, 2000). In Spain spatial planning of flood areas is included in the Water Act and institutional regulations (Menendez, 2000). Switzerland heavily engages in mapping activities to identify zones that are prone to natural hazards (e.g., Petraschek, 2002). In Norway maps are created for six different flood levels (HQ10/20/50/100/200/500) following uniform technical guidelines (Hoydal et al., 2002). In Austria hazard zone maps are developed at a scale of 1 : 2000, in which three zones (red, yellow and blue) are distinguished (RIWA-T, 2006). Red zones are determined by a velocity-depth criterion, whereas yellow zones are bounded by the extent of a hundred-years flood. Blue zones exhibit areas of specific flood management. Additionally, rest risk areas (HQ300) and the spatial extent of the thirty year event (HQ30) are presented in Austrian flood hazard mapping (RIWA-T, 2006). Given the importance of event simulations for planning, their quality is crucial.

The most influential input parameters for HN models are the topography provided as a Digital Terrain Model of the Watercourse (DTM-W) and the flow resistances usually provided as roughness coefficients. According to technical advances in computer aided hydrodynamic-numerical modelling and the related multidimensional (2-D/3-D)

applications, the need for high quality 3-D terrain data is increasing (Sinha et al., 1998). Airborne LiDAR (Light Detection and Ranging) provides high point density and remarkable height precision (Csanyi and Toth, 2007). It is especially well suited for capturing flood plains as well as river banks under low flow conditions and is therefore widely
⁵ used as data basis for HN models.

However, the application of LiDAR poses problems as well. Contrary to traditional manual data acquisition techniques like stereo-photogrammetry or tachymetry, LiDAR comprise both terrain and off-terrain points on buildings, vegetation, power lines, etc. The quality of the derived DTM and, consequently, the quality of subsequent HN mod-
¹⁰ elling depends crucially on how well off-terrain points have been eliminated within the filtering process. Another issue besides filtering is the fusion of LiDAR and river bed data. This involves the derivation of the water-land-boundary and the interpolation of river bed cross sections.

Nowadays, most HN models are solved using a Finite Element (FE) or Finite Volume
¹⁵ (FV) approach on the basis of unstructured or hybrid geometries, i.e. a computation grid based on irregularly distributed points. Many hydraulic mesh generators are available, which build up a network mainly of triangles and quadrilaterals covering the entire project area. These mesh generators consider hydraulic parameters like angle criterion and aspect ratio, but normally disregard topographic details as contained in data from
²⁰ modern LiDAR sensors. The heights are mapped to the hydraulic grid a posteriori. Many modelling tools can only handle a limited number of points and elements (Nujic, 1999). Thus, the direct use of the high resolution LiDAR DTM as computation grid is impossible due to the enormous amount of data.

This article presents a new method for constructing hydraulic computation grids by
²⁵ preserving geometric surface details as well as considering physical mesh quality parameters. An adaptive TIN refinement method is used to thin out the high resolution LiDAR DTM, which is professionally conditioned in a subsequent postprocessing step to meet the required mesh quality parameters. The method, thus, overcomes the limitations of mesh generation approaches considering physical parameters only.

Optimisation of LiDAR DTMs for river flow modelling

G. Mandlburger et al.

Title Page

Abstract	Introduction
Conclusions	References
Tables	Figures

|◄ | ►|
◄ | ►

Back | Close

Full Screen / Esc

Printer-friendly Version

Interactive Discussion

Optimisation of LiDAR DTMs for river flow modelling

G. Mandlburger et al.

In the following Sect. 2 the study area and data sets are introduced. Thereafter, the major steps of the proposed workflow are described in detail, comprising LiDAR DTM processing (Sect. 3), DTM data reduction and conditioning (Sect. 4) and hydrodynamic-numerical modelling (Sect. 5). The results and application examples are presented and discussed in the subsequent Sects. 6 and 7. The final section concludes the major findings and points out the benefits of our approach.

2   Study area and data sets

Special meteorological conditions in Lower Austria and the south of the Czech Republic were responsible for an extreme flood in summer 2002 at the river Kamp (Gutknecht et al., 2002). A precipitation event of 150–370 mm was documented in the first 12 days of August 2002, 3–4 times higher than the average monthly precipitation in the catchment area of the river Kamp (Holzmann, 2002). These massive rainfalls caused a flood with two distinct peaks. The first flood wave occurred on 8 August (cf. Fig. 1). Within 24 h the discharge increased from 100 m^3/s to 800 m^3/s (gauging station Stiefern, HQ100 at Stiefern: 490 m^3/s). The recorded discharges were nearly twice as high as the 100-year event for gauging station Stiefern (estimated return period 500–2000 years). On 14 August the second wave occurred with a maximum discharge of about 500 m^3/s. During the flood in the Kamp valley chute cut-offs and floodplain stripping occurred and local overbank scours were documented.

The study reach is a 2 km section midstream of the river Kamp situated in the northern part of Lower Austria at the village Gars am Kamp (Fig. 2). The origin of the river Kamp is near the village Karlstift and after a 160 km long course it discharges into the Danube River (182 m a.m.s.l.) at Altenwörth. The total catchment area measures 1753 km^2 and the hydrologic regime is described as pluvio-nival (Mader et al., 1996) with an average annual precipitation of 900 mm. The average bed slope of the selected study reach is approx. 2.5 ‰. The investigated river section of Gars am Kamp was heavily affected by the catastrophic flooding in August 2002. A high percentage

of buildings (20.1%, 293 of 1460) were damaged or even destroyed. As entire losses a sum of more than 13 million € was reported by the Lower Austrian Federal Government (Habersack et al., 2004).

As a result of the extreme 2002 flood event a LiDAR campaign was carried out for the entire Kamp valley. The data was captured during 25 November 2002 and 2 March 2003 by company TopoSys (TopoSys, 2008) using a Falcon II sensor at an average flying altitude of 850 m above ground. The reported accuracy of the captured 3-D-points was ±0.5 m in planimetry and better than ±0.15 m in height. The Falcon II scanner measures at a pulse repetition rate of 83 kHz. The scanner is mounted on an oscillating platform, which produces a meandering scan pattern on the ground to improve the inhomogeneous point distribution of the scanner (more points in scan direction than in flight direction). First echoes and last echoes together with their signal amplitude were recorded at an average point density of 1 point/m^2. From the original point recordings a Digital Surface Model (DSM, cf. Fig. 2c) consisting of approx. 1.16 million points for the entire study reach and 700.000 terrain points were derived. Additionally to the LiDAR points, cross sections at an average distance of 60 m were captured by terrestrial survey to describe the topography of the river bed.

3 LiDAR DTM processing

In this section the state of the art in DTM acquisition in general and obtaining terrain models from airborne LiDAR in particular will be reviewed.

For the specification of terrain surface products the Digital Terrain Elevation Data (DTED) levels from 1 to 5 have been suggested. For HN simulations especially the resolution and accuracy levels are of interest. Level 2 is fulfilled by DTMs with a horizontal resolution (grid edge length) of 1″ (approx. 20–30 m) and an absolute vertical accuracy of 18 m (90% error bound). It may be reached by spaceborne Interferometric Synthetic Aperture Radar (InSAR) using the X-band (e.g. SRTM, Rabus et al., 2003), which is, however, scattered back at the tree crowns. Level 3, also referred to as High Resolution

Terrain Information (HRTI-3), with 12 m resolution and 10 m accuracy, is aimed at by new satellite InSAR missions (Krieger et al., 2007). HRTI-4 (6 m resolution, 5 m accuracy) can be achieved by airborne InSAR and stereo photogrammetry (Kraus, 2007). At this level it makes a notable difference if the ground surface is recorded or the first visible surface from the bird's perspective (tree crowns, roofs, etc.). Short wavelength radar and passive optical imaging can provide high resolution, but cannot take measurements from the ground surface below the forest cover (Baltsavias et al., 2008). HRTI-5 can currently only be provided by airborne LiDAR for larger areas in a cost efficient manner and prescribes a resolution of 1 m, an absolute vertical accuracy of 5 m, and a relative (point-to-point) precision of 25 cm. Especially the accuracy requirements are the fact advocating for airborne LiDAR.

In airborne LiDAR the travel time of a short pulse of laser energy from the sensor to the ground surface and back is measured. The position and orientation of the sensor platform is determined with GPS and IMU (Global Positioning System, Inertial Measurement Unit). The laser pulse can "see" through small gaps in the foliage and travel to the ground below the tree canopy. The result is a cloud of points originating from the ground surface and the canopy in a forest environment. In open areas the points are only lying on the ground surface. The task of separating the points on the ground surface from the other, off-terrain points is called filtering (Kraus and Pfeifer, 1998). Different approaches have been suggested (Pfeifer and Mandlburger, 2008) making different assumptions on the terrain surface and either processing by gradually adding or gradually removing unclassified points. Finally, advanced algorithms also consider the random measurement noise.

The methods of mathematical morphology (Kilian et al., 1996; Vosselman, 2000; Zhang et al., 2003) classify points depending on vertical and horizontal distances between points. The principle is that a large height difference at small horizontal distance can only occur, if the higher point is off the ground. In progressive densification (von Hansen and Vögtle, 1999; Axelsson, 2000; Sohn and Dowman, 2002) the terrain surface is described by a triangulation, that is gradually built up. Starting from a few known

Optimisation of LiDAR DTMs for river flow modelling

G. Mandlburger et al.

Full Screen / Esc

Printer-friendly Version

Interactive Discussion

terrain points, new points are added, if they are within certain distances from the triangulation surface. With these algorithms also a notion of surface is introduced. In robust interpolation (Kraus and Pfeifer, 1998) a surface model is interpolated starting from all points, more precisely approximating all points, e.g. by linear prediction or kriging
5 (Kraus, 2000; Journel and Huijbregts, 1978). This surface model runs in an averaging way between terrain and off-terrain points. The residuals, i.e. the vertical distances from the measurements to the surface model, are computed and become input for a weight function. This way, high weights are associated with points below the current surface, and small weights with points above it. These weights are considered in the
10 next iteration step of surface computation. Points with larger weights attract the surface, while points with lower weights have less and less influence in subsequent iterations. The approach has been embedded in a hierarchic setup, for increasing robustness and efficiency (Pfeifer et al., 2001). A comparable method has been suggested by Elmqvist et al. (2001). The advantage of this approach is that the surface properties,
15 expressed e.g. by the variogram of kriging, are clearly separated from the properties of LiDAR data (terrain and off-terrain points), which are expressed in the weight function. Random measurement errors are considered, if a suitable surface interpolation technique like linear prediction is chosen. Finally, segmentation approaches were suggested (Sithole and Vosselman, 2005; Nardinocchi et al., 2003; Tóvari and Pfeifer,
20 2005) for separating terrain and off-terrain points, which first group the points to larger entities (e.g. planar areas) and then classify those. They are mainly advantageous in city areas, where a large number of well-defined, planar surfaces do exist.

As reported in a comparison of filter algorithms (Sithole and Vosselman, 2004) all filters have their problems at step edges. As shown by Doneus and Briese (2006)
25 also low vegetation can be very problematic for correctly identifying the terrain points automatically. With the advent of commercial full-waveform LiDAR systems (Wagner et al., 2004) a step forward in filtering became possible. In full-waveform LiDAR not only the travel time of the pulse is recorded, but the entire shape of the backscattered echo is digitised. In open areas the ground surface is well-defined and the emitted shot

of laser energy is scattered back undistorted. For vegetation, however, the situation is different. The "surface" of bushes or tree crowns is vertically much more extended with respect to the laser footprint (50 cm–1 m), backscattered echoes are therefore widened. This can be used as a pre-classifier to detect points lying on the vegetation,
5 and, ground detection becomes more robust and accurate (Doneus and Briese, 2006).

4 DTM data reduction and conditioning

4.1 DTM data reduction

Modern LiDAR sensors allow mapping of topographic details at the price of a highly increased data volume. In order to obtain a manageable amount of data for FE meshes
10 used in HN modeling data reduction and surface simplification is inevitable. The main goal is to reduce the vertices of the DTM (grid points, breaklines, etc.) without losing relevant geometric details.

For polygonal simplification of 2.5-D surfaces mainly regular grid algorithms, decimation and refinement techniques are in use (Heckbert and Garland, 1997). The
15 regular grid approaches are widespread, simple and fast, but they are not adaptive and produce poor approximation results. Better approximation quality can be achieved by applying decimation and refinement methods based on general triangulation algorithms such as Delaunay triangulation. Decimation methods work from fine-to-coarse and are not suited for processing large high resolution LiDAR DTMs since they require
20 a triangulation of the entire point set. Refinement methods represent a coarse-to-fine approach starting with a minimal initial approximation. In each subsequent pass one or more points are added as vertices to the triangulation until the desired approximation tolerance is met or the desired number of vertices is used.

The performance of DTM data reduction is highly influenced by the existence of
25 systematic and random measurement errors. For deriving thinned DTM models from original LiDAR point clouds, directly using refinement or decimation approaches as de-

scribed above are not the first choice. Systematic errors have to be removed first by exact sensor calibration and fine adjustment of the LiDAR-strip data (Schenk, 2001; Filin, 2003; Kager, 2004). The random measurement errors of the LiDAR points should rather be eliminated by applying a DTM interpolation strategy with measurement noise
5   filtering capabilities such as linear prediction (Kraus, 2000) or kriging (Journel and Hui-jbregts, 1978). High reduction ratios can only be achieved for DTMs, where systematic errors have been strictly eliminated and random errors have been smoothed during surface interpolation.

In contrast to approaches which rely on the original point cloud, our adaptive TIN
10 refinement approach uses the filtered hybrid DTM (regular grid and breaklines, structure lines, and spot heights) as input (Mandlburger, 2006). The basic parameters for the DTM simplification are a maximum height error Δz_{max} (L_∞-norm) and a maximum planimetric point distance Δxy_{max}. The latter avoids triangles with too long edges and narrow angles. The algorithm starts with an initial approximation of the DTM com-
15 prising all structure lines and a coarse regular grid (cellsize=Δxy_{max}=Δ_0), which are triangulated using a Constrained Delaunay Triangulation. Each Δ_0-cell is subsequently refined by iteratively inserting additional grid points until the height tolerance Δz_{max} is achieved.

The additional vertices can either be inserted hierarchically or irregularly. In case of
20 hierarchical breakdown, we use a coarse rectangular grid as initial surface approximation. Each coarse grid cell is divided into four parts in each pass, if a single grid point within the regarded area exceeds the maximum tolerance. This leads to a quad-tree like point distribution in the resulting surface approximation. By contrast, for irregular division a regular grid of (approximately) equilateral triangles is used as initial approx-
25 imation. This is especially suited for FE-meshes since the connecting line of adjacent cell centers (i.e. direction of calculation) always intersects the joint cell boundary at a right angle. In a single pass the grid points with the maximum positive and maximum negative deviation are inserted (parallel greedy insertion). Furthermore, the process of point insertion and recalculation of the error measures is optimised by considering

the locality of the mesh changes. Higher compression ratios (up to 99% in flat areas) can be achieved with irregular point insertion, whereas the hierarchical mode is characterised by a more homogeneous data distribution. Using the terms of hydraulics, the hierarchic division produces an adaptive cartesian grid whereas irregular division yields an unstructured grid.

The described framework is flexible concerning the reduction criterion. The decision to insert a point can be based on the analysis of the local surface slope and the curvature derived from the DTM or on the vertical distance between the DTM point and the approximating TIN.

4.2 Data conditioning

To get a high quality computation grid for HN modelling, the simplified polygonal surface mesh has to be conditioned considering the physical phenomena being simulated (flow direction, bottom shear stress, . . .). According to Ferziger and Peric (2002) the main quality parameters for a good FE grid are: (i) angle criterion, (ii) aspect ratio and (iii) expansion ratio. The aspect ratio describes the proportion of the longest and shortest edge within a mesh face, whereas the expansion ratio is a measure describing the area ratio between adjacent meshes. Requirements concerning angles in a computational mesh appear in two different ways. First, the angles between the mesh edges and, second, the alignment of the cells with respect to the direction of force have to be considered. In a nutshell, small angles of less than $<10°$ should be avoided, the cells should be aligned to the principal flow direction, the aspect ratio should not exceed 10 (optimum<3) and the expansion ratio must not be greater than 3 (optimum<1.2).

Thus, to achieve physically reliable results the cells of the computation mesh have to be aligned alongside the current for the entire wetted perimeter of a river under high flow conditions. This applies for the river bed and the river bank. The river axis can serve as a sufficient approximation of the principle flow direction. Quadrilateral cells with the longer sides in and the shorter ones perpendicular to the flow direction with edge length proportional to 3:1 (optimum aspect ratio) have turned out to produce good

simulations results (Mandlburger, 2006). Beyond the embankment, the flow directions are no longer strictly parallel, thus, irregular data distribution as described in the previous subsection is appropriate. However, especially for flood mapping different zones can be designated within the inundation area depending on the respective vulnerabil-

5 ity. Residential areas in the vicinity of a river, for instance, should be mapped in more detail than remote or elevated areas. The concept of varying mapping precisions can be applied to the DTM simplification approach by introducing spatially varying maximum height tolerances. Mathematically the tolerances can be expressed as a bivariate function ($\Delta z_{max} = f(x, y)$). Distances from the river bank or relative height differences

10 respectively can be used to control the tolerances, but a simple zonal model has turned out to be suited best. The delineation of the different accuracy zones can be derived from a pilot survey (e.g. a preliminary 1-D-CFD simulation), from DTM visualisations such as hill shadings, from existing maps or the like.

Finally, the resulting TIN has to be analysed with respect to the adherence of angle

15 criterion, aspect and expansion ratio. Therefore, the entire triangulation is traversed and, if necessary, additional vertices are inserted or unessential vertices are removed. The results of a simplified DTM grid, professionally conditioned to preserve geometric details and fulfill physical quality criterions, is shown in Fig. 4.

5 Hydrodynamic-numerical modelling

20 To evaluate the impact concerning the availability of geometric details on the results of river flow simulations, the two-dimensional depth-averaged hydrodynamic-numerical model Hydro_AS-2-D (Nujic, 1999) was applied in the study reach. Basic principles of two-dimensional mathematical flow modelling are the 2-D depth-averaged equations (simplified Navier-Stokes-equations), also referred to as shallow-water equations.

25 Within the Hydro_AS-2-D model the shallow water equations are spatially discretised based on the finite volume approach. Simplified in vector form the shallow water equa-

tion can be described as follows:

$$\frac{\partial \boldsymbol{w}}{\partial t} + \frac{\partial \boldsymbol{f}}{\partial x} + \frac{\partial \boldsymbol{g}}{\partial y} + \boldsymbol{s} = 0 \tag{1}$$

where:

$$\boldsymbol{w} = \begin{pmatrix} H \\ uh \\ vh \end{pmatrix}, \quad \boldsymbol{f} = \begin{pmatrix} uh \\ u^2 h + \frac{gh^2}{2} - vh\frac{\partial u}{\partial x} \\ uvh - vh\frac{\partial v}{\partial x} \end{pmatrix},$$

$$\boldsymbol{s} = \begin{pmatrix} 0 \\ gh(I_{Rx} - I_{Sx}) \\ gh(I_{Ry} - I_{Sy}) \end{pmatrix}, \quad \boldsymbol{g} = \begin{pmatrix} vh \\ uvh - vh\frac{\partial u}{\partial y} \\ v^2 h + \frac{gh^2}{2} - vh\frac{\partial v}{\partial y} \end{pmatrix}$$

H is the water surface elevation [m], the sum of the water depth (h) and the terrain height (z). u and v are the velocities in x- and y-direction [m/s], g the acceleration due to gravity [m/s^2] and v the kinematic viscosity term [m^2/s].

$$I_{Rx} = \frac{\lambda u \sqrt{u^2 + v^2}}{2gD}, I_{Ry} = \frac{\lambda v \sqrt{u^2 + v^2}}{2gD}, I_{Sx} = -\frac{\partial z}{\partial x}, I_{Sy} = -\frac{\partial z}{\partial y} \tag{2}$$

$$\lambda = 6.34 \frac{2gn^2}{\sqrt[3]{D}} \tag{3}$$

where, n is the Manning coefficient [$\frac{s}{\sqrt[3]{m}}$], D the hydraulic diameter $4R_{hy}$ [m], $R_{hy}=H=$water depth [m].

Hydro_AS-2-D uses the Surface water Modelling System (SMS) as a pre- and post-processing tool. The convective flow of the two-dimensional model is based on the Upwind-scheme by Pironneau (1989) and the discretisation of time is done by an explicit Runge Kutta method in second order. Several methods for implementing viscosity

in numerical modelling exist. In the applied Hydro_AS-2-D model the viscosity is calculated based on a combination of empirical and constant viscosity approaches.

$$\nu = \nu_0 c_\mu v^* h \tag{4}$$

where c_μ is the viscosity parameter and v^* the shear velocity [m/s].

For the simulations in this case study a viscosity coefficient of c_μ=0.6 was used, the computation time was set to 32 000 s to achieve steady state conditions and the depth criterion for wetting/drying computations was set to 0.01 m The hundred-years flood (Gars: 470 m^3/s) was used as input discharge (boundary condition) being the most important design discharge for hazard zone mapping in Austria (RIWA-T, 2006). Separate roughness n-values were determined for the main channel and for overbank areas. Whereas main channel roughness coefficients were calibrated on the basis of field measurements (flow velocities and water surface elevations of a HQ30), only a single value (n=0.04) was used for the study reach floodplains to best exhibit the influence of different geometries on flood level and flood hydraulics. It was not the aim of the presented paper to achieve realistic flood stages for the hundred-years event by calibrating different overbank parameters (e.g. vegetation, land use, ...).

6 Results

Before running the hydrodynamic-numerical simulation we had to build up a precise LiDAR based DTM-W covering the wetted perimeter of a HQ100 at least and including the river bed and all flow prohibiting buildings. Our data basis comprised the LiDAR points aligned in a 1 m raster, the river bed cross sections (terrestrial survey) and 2-D building polygons (cadastral map). In a first step, we derived a DTM of the overbank areas without gaps. Since the LiDAR terrain points at hand were sparsely distributed due to prior filtering, we merged all terrain and DSM points and analysed the point cloud with SCOP++ (SCOP++, 2008), which implements the hierarchic robust interpolation

(cf. Sect. 3). Thereafter, we derived the water-land-boundary as described in Brock-mann and Mandlburger (2001) serving as clipping polygon to cut out all laser echoes within the river bed. The bed surface itself was subsequently constructed by densi-fying the cross sections using an interpolation approach, which considers the curved
5 progression of the river axis (Mandlburger, 2000). To reflect the natural flow conditions in our geometry model as realistically as possible, we decided to include the build-ings as block models in the DTM-W. Therefore, we used 2-D building polygons from the cadastral map and estimated an average height for each building. The resulting 3-D polygons were introduced to the DTM-W in a final step, where we interpolated all
10 preprocessed data (i.e. classified LiDAR terrain points and densified river bed points) using linear prediction (Kraus, 2000). Thus, random measurement errors in the height component in the order of ±15 cm were considered in the DTM computation. A grid with an edge length of 1 m containing additional breaklines was derived and the result-ing hybrid DTM-W is illustrated in Fig. 3. Virtually all the tasks mentioned above were
15 carried out using the SCOP++ software developed at the Institute of Photogrammetry and Remote Sensing, Vienna.

Additionally, data reduction and conditioning was performed as described in Sect. 4. We chose a maximum height tolerance $\Delta z_{max}=\pm20$ cm and started the TIN refinement process with a basic triangular point pattern (edge length $\Delta_0=16$ m). The irregular
20 TIN of the river bed was automatically replaced by cell elements aligned to the flow direction. The resulting professionally thinned and conditioned DTM-W grid, which can be used as hydraulic computation mesh straightforward, is shown in Fig. 4.

To estimate the impact of additional geometry details provided by LiDAR on instream hydraulics, numerical simulations for HQ100 were carried out for two different geome-
25 try variants. We compared a low resolution geometry (a) to a very detailed description of the terrain (b). Geometry (a) consists of a regular 20 m grid. The spatial resolution conforms to DTED Level 2, which can be achieved using spaceborne remote sens-ing techniques like InSAR (e.g. SRTM). Anyway, the deployed 20 m grid was derived from LiDAR via static grid reduction (low pass filtering). In a preprocessing step the

coarse grid was augmented by additional breaklines from terrestrial survey to improve the description of the river banks and weir channels. By contrast, geometry (b) was derived from the precise 1 m LiDAR DTM-W as a hybrid computation grid (floodplain: unstructured grid, river bed: structured grid) as described above. The two different grid variants are illustrated in Fig. 5.

For the investigated 2 km river reach geometry (a) featured a total number of 6602 nodes (39 384 triangular or quadrilateral surface elements) whereas geometry (b) consists of 96 225 nodes (191 229 surface elements). The 1m LiDAR DTM contains a total number of 1.16 million grid posts and 20 600 breakline points (building terrain intersections and eaves). Thus, for geometry (a) only 0.5% of the available data source are utilised to describe the terrain geometry and, therefore, many surface details are lost. For geometry (b) 8% of the LiDAR DTM posts are necessary to describe the terrain surface with a maximum approximation tolerance $\Delta z_{max} = \pm 20$ cm.

The most important results of hydraulic simulations are water depths, flow velocities and flow direction vectors. Based on these parameters water surface levels, flood extents and bottom shear stresses are derived. Figure 6 contains a map of water depths and flood boundaries for the same section and the same geometry variants as shown in Fig. 5. A remarkable difference of the flood extent between model (a) and (b) can be observed, especially close to the railway dam and the road dams. These geometric details are contained in model (b) only. They restrict the inundated area whereas the flooded area exceeds beyond the dams in model (a). The consequences of the restricted run-off area in model (b) are illustrated in Fig. 7. It can be seen that the flow velocities in the main channel are higher in model (b) than in model (a).

A quantitative comparison of the velocity differences of both model variants was carried out for a 215 m long section along the center line of the river Kamp close to the Dungl hotel. The profile outline is plotted in Fig. 7, whereas the velocity profile itself is illustrated in Fig. 8. The mean velocity in model (a) is 2.17 m/s (sample size $n=45$) and 3.17 m/s ($n=97$) in model (b). The difference of the mean velocities between model (a) and (b) is statistically significant with respect to a 95% confidence interval ($p=0.0$).

Optimisation of LiDAR DTMs for river flow modelling

G. Mandlburger et al.

Figure 8 illustrates the progression of the flow velocity and bottom shear stress (i.e. parameter for erosion and deposition of sediments) along the longitudinal section. Both parameters show a similar progression in both geometry variants with greater values in model (b) than in model (a). The maximum bottom shear stress values are 129 N/m^2 in (a) and 211 N/m^2 in (b) which represents a relative increase of +63% of model (b) compared to (a).

Finally, the cross section plotted in Fig. 7 was examined in detail and the results concerning water depth, flow velocity and bottom shear stress are illustrated in Fig. 9. The water depth of both model variants exhibit only small deviations in the range of a few centimeters. However, an increase of the flow velocity can be observed in model (b) within the main channel, which is compensated by lower flow velocities in the over bank areas. Model (a) shows a reciprocal progression with lower velocities in the main channel and higher values in the foreland. At station 150 m, for instance, the velocity adds up to 0.76 m/s in model (a) and only 0.21 m/s in (b). Furthermore, an interesting detail can be observed at the location of the Dungl hotel. Since the buildings are contained in the computation grid of model (b) in a generalised way, the water depth, velocity and bottom shear stress go down to zero. These details are not reflected in the coarser model (a).

7 Discussion

Due to the fact, that LiDAR based hydraulic modelling can be seen as state of the art in hazard zone mapping, it should be highlighted that precise and reliable modelling results (i.e. flood extents ...) can only be achieved by exploiting the full potential of the LiDAR data concerning accuracy and resolution. The progress in computing power and hydraulic modelling software enables the application of more complex geometries as provided by LiDAR. The results described in the previous section made clear, that the consideration of a more detailed geometry has significant impact on the hydraulic modelling results, not only concerning the flood extent but, above all, regarding the dis-

Title Page

Abstract | Introduction

Conclusions | References

Tables | Figures

|◄ | ►|

◄ | ►

Back | Close

Full Screen / Esc

Printer-friendly Version

Interactive Discussion

tribution of flow velocities and bottom shear stresses. The latter are equally important for estimating the risk potential in hazard zone mapping. In the following the results stated above are discussed critically in detail.

The potential discharge area in the village Gars is restricted by the railway dam (right bank) and road dams (left bank). For the 100-year flood event the dams act as a flow barrier in model (b) since they are reflected sufficiently in the computation grid whereas the coarser geometry approximation of model (a) allows overtopping of the dams and, therefore, inundating of large flood plain areas beyond the dams. Proper consideration of the dams requires a certain ground resolution of the topographic data acquisition. A resolution of 20–30 m, that can be achieved using spaceborne InSAR techniques is, therefore, not sufficient for precise hazard zone mapping. Airborne LiDAR, in contrast, is well suited both concerning the required planimetric resolution of approx. 1 m and height accuracy better than 20 cm. The relevant flow restricting features can be considered in the computation grid either by means of a higher point density at the base and top of the dams or through including the dam breaklines as constraints in the mesh. It has to be mentioned, that in case of the reported 2002 flood the entire area of Gars including the flood plains beyond the dams were inundated, but the discharge of this extreme event was by far higher than the HQ100 discharge for which the simulations at hand were carried out. Furthermore, it should be stressed that the dams were treated as watertight in the simulations, i.e. no culverts were considered. Anyway, openings in dams are nowadays more and more safeguarded by mobile flood control measures.

The restriction of the discharge area by dams and buildings as provided by geometry (b) entails a discharge concentration in and near the main channel. As a consequence, higher flow velocities and bottom shear stresses can be observed there. The significant increase of the bottom shear stress (+63% compared to model (a)) represents a severe issue for the structural integrity of projected flood safety measures as well as existing buildings. Many cases of dam breaks and undermining of building foundations were reported in the recent past (Habersack and Krapesch, 2006).

The cross-sectional comparisons of flow velocity and bottom shear stress have

shown a decrease of these parameters in the precise model variant (b) compared to the coarse model (a) for overbank areas. Maximum bottom shear stress values of up to $10\,\mathrm{N/m^2}$ can be observed in model (a), whereas the values are five times lower (approx. 1–$2\,\mathrm{N/m^2}$) in (b). Low bottom shear stress entails a sedimentation of transported suspended loads. Siltation processes, in turn, can be observed at virtually every flood event and provoke a high vulnerability particularly for residential areas. Therefore, a correct estimation of flow velocities and bottom shear stresses in hydraulic models can be regarded as equally important as a precise estimation of the flood extent. This becomes even more relevant when using flood hydraulics as boundaries for suspended- and bed load transport modelling. The comparison of the simulation results at hand has shown the high impact of the detailed LiDAR based geometry description (b) especially on flow velocity and bottom shear stress. It can be stated that a correct representation of these hydraulic modelling parameters can only be achieved on the basis of a precise and detailed description of the geometry.

8 Conclusions

In this article a method for the generation of a hydraulic grid was presented. It starts from a digital terrain model in the form of a regular or hybrid grid, which is derived from airborne LiDAR point clouds by a method considering the random measurement errors. An irregular thinning scheme allows deriving an irregular triangular mesh with a defined tolerance compared to the original DTM. In the example presented, the point set describing the terrain was reduced to less than 8% in comparison to the original point cloud and the regular DTM grid. The obtained triangular mesh is conditioned by inserting vertices in order to assure that the hydrodynamic numerical simulations can be solved.

Airborne LiDAR allows identifying vegetated areas and buildings. The properties of LiDAR even enable retrieving terrain point measurements below the forest cover and, thus, enable obtaining accurate terrain models. The identified building blocks, in turn,

can be inserted into the grid for flood event simulation.

A flood event simulation on a grid according to the proposed method was compared to a simulation on a regular hydraulic grid featuring a resolution in the order of 20 m. Elevation data with similar resolutions are available publicly (e.g. SRTM). New space-borne satellite missions aim at resolutions of a few meter, but the accuracy of airborne LiDAR will not be reached. Additionally, as short wavelengths (X-band) are used, no terrain below forest canopy can be derived.

The two event simulations were similar with respect to their water surface levels but showed remarkable differences concerning the flooded area, flow velocity, etc. Comparisons to real floodings (e.g. suspended sediment deposition, side erosion processes) indicate, that the simulation on the basis of the low resolution elevation information is not realistic.

We conclude therefore that (i) airborne LiDAR is the method of first choice for topographic data acquisition of floodplains, and (ii) that the method of first reducing random measurement errors and subsequently applying irregular thinning in overbank areas and cell arrangement with respect to the flow direction in the river bed leads to meshes, that need little conditioning and can be input for HN analysis. This asserts that the geometric information captured by airborne LiDAR is in its essence available for hydrodynamic-numerical simulations.

References

Axelsson, P.: DEM generation from laser scanner data using adaptive TIN models, in: International Archives of Photogrammetry and Remote Sensing, XXXIII, B4, 111–118, Amsterdam, Netherlands, 2000. 3611

Baltsavias, E., Gruen, A., Eisenbeiss, H., Zhang, L., and Waser, L. T.: High-quality image matching and automated generation of 3D tree models, Int. J. Remote Sens., 29, 1243–1259, 2008. 3611

BEV: Bundesamt für Eich- und Vermessungswesen, http://www.bev.gv.at/, 2008. 3624

5   Brockmann, H. and Mandlburger, G.: Modelling a watercourse DTM based on airborne laser-scanner data – using the example of the River Oder along the German/Polish Border, in: Proceedings of OEEPE Workshop on Airborne Laserscanning and Interferometric SAR for Detailed Digital Terrain Models, Stockholm, Sweden, 2001. 3619

Csanyi, N. and Toth, C.: Improvement of Lidar data accuracy using lidar-specific ground targets,
10   Photogramm. Eng. Rem. S., 73, 385–396, 2007. 3608

Denoth, S.: Zweidimensionale Hochwassersimulation der Elbe zwischen Torgau und Coswig, Diplomarbeit, Institut für Hydromechanik und Wasserwirtschaft, ETH Zürich, 2003. 3607

Doneus, M. and Briese, C.: Digital terrain modelling for archaeological interpretation within forested areas using full-waveform laserscanning, in: The 7th International Symposium on
15   Virtual Reality, Archaeology and Cultural Heritage VAST, Zypern, 2006. 3612, 3613

Elmqvist, M., Jungert, E., Lantz, F., Persson, A., and Söderman, U.: Terrain modelling and analysis using laser scanner data, in: International Archives of Photogrammetry and Remote Sensing, XXXIV, 3/W4, Annapolis, MD, USA, 2001. 3612

EVN: Energieversorgung Niederösterreich AG: http://www.evn.at/, 2008. 3624

20   Ferziger, J. H. and Peric, M.: Computational Methods for Fluid Dynamics, Springer, Berlin, 3 Ed., 2002. 3615

Filin, S.: Recovery of systematic biases in laser altimetry data using natural surfaces, Photogramm. Eng. Rem. S., 69, 1235–1242, 2003. 3614

Fischer-Antze, T., Stoesser, T., Bates, P., and Olsen, N.: 3D numerical modelling of open
25   channel flow with submerged vegetation, J. Hydraul. Res., 39, 303–310, 2001. 3607

Gouda, M., Karner, K., and Tatschl, R.: Dam flooding simulation using advanced CFD methods, in: Proceedings of the Fifth World Congress on Computational Mechanics, Vienna, Austria, 2002. 3607

Gutknecht, D., Reszler, C., and Blöschl, G.: The August 7, 2002 – flood of the Kamp – a first
30   assessment, Elektrotechnik und Informationstechnik, 119, 411–413, 2002. 3609

Habersack, H. and Gaul, A. (eds.): Fließgewässermodellierung – Arbeitsbehelf Hydrodynamik, Nr. 37, Österreichische Wasser- und Abfallwirtschaftsverband, Vienna, Austria, 2008. 3607

Habersack, H. and Krapesch, G.: Hochwasser 2005 – Teilbericht der Bundeswasserbauver-

HESSD

5, 3605–3638, 2008

Optimisation of LiDAR DTMs for river flow modelling

G. Mandlburger et al.

Title Page

Abstract	Introduction
Conclusions	References
Tables	Figures

|◄ | ►|

◄ | ►

Back | Close

Full Screen / Esc

Printer-friendly Version

Interactive Discussion

waltung, Bundesministerium für Land- und Forstwirtschaft, Umwelt und Wasserwirtschaft, Universität für Bodenkultur, Wien, 2006. 3622

Habersack, H., Bürgel, J., and Petraschek, A.: Analyse der Hochwasserereignisse vom August 2002, floodrisk, Synthesebericht., 2004. 3610

5 Hauer, C., Mandlburger, G., and Habersack, H.: Hydraulically related hydro-morphological units: description based on a new conceptual mesohabitat evaluation model (MEM) using LiDAR data as geometric input, River Res. Appl., 279–296, available at: http://www3. interscience.wiley.com/journal/117953086/abstract, 2008a. 3607

Hauer, C., Unfer, G., Schmutz, S., and Habersack, H.: Morphodynamic Effects on the Habitat 10 of Juvenile Cyprinids (Chondrostoma nasus) in a restored Austrian Lowland River, Environ. Manage., 42, 279–296, 2008b. 3607

Heckbert, P. S. and Garland, M.: Survey of Polygonal Surface Simplification Algorithms, Tech. rep., School of Computer Science, Carnegie Mellon University, Pittsburgh, PA, Technical Report, 1997. 3613

15 Holzmann, H.: Ereignisdokumentation Hochwasser August 2002, aP-Hydrologie, Habersack & Moser, 2002. 3609

Hoydal, O. A., Berg, H., Haddenland, I., Petterson, L. E., Vosko, A., and Oydvin, E.: Procedures and guidelines for flood inundation maps in Norway, Norwegian Water and Energy Directorate, 404–410, 2002. 3607

20 Journel, A. G. and Huijbregts, C. J.: Mining Geostatistics, Academic Press, New York, 1978. 3612, 3614

Kager, H.: Discrepancies Between Overlapping Laser Scanning Strips – Simultaneous Fitting of Aerial Laser Scanner Strips, in: International Archives of Photogrammetry and Remote Sensing, XXXV, B/1, 555–560, Istanbul, Turkey, 2004. 3614

25 Khan, A. A. and Barkdoll, B.: Two-Dimensional Depth-Averaged Models for Flow Simulation in River Bends, Int. J. Comput. Eng. Sci., 2, 453–467, 2000. 3607

Kilian, J., Haala, N., and Englich, M.: Capture and evaluation of airborne laser scanner data, in: International Archives of Photogrammetry and Remote Sensing, XXXI, B3, 383–388, Vienna, Austria, 1996. 3611

30 Kraus, K.: Photogrammetrie, Band 3, Topographische Informationssysteme, Dümmler, 2000. 3612, 3614, 3619

Kraus, K.: Photogrammetry – Geometry from Images and Laser Scans, de Gruyter, 2 Ed., 2007. 3611

Kraus, K. and Pfeifer, N.: Determination of Terrain Models in Wooded Areas with Airborne Laser Scanner Data, ISPRS J. Photogramm. Rem. S., 53, 193–203, 1998. 3611, 3612

Krieger, G., Moreira, A., Fiedler, H., Hajnsek, I., Werner, M., Younis, M., and Zink, M.: TanDEM-X: A Satellite Formation for High-Resolution SAR Interferometry, IEEE T. Geosci. Remote, 45, 3317–3341, 2007. 3611

Mader, H., Steidl, T., and Wimmer, R.: Klimatologisch-Hydrologische Typisierung der Österreichischen Fließgewässer, Umweltbundesamt, Wien, 1996. 3609

Mandlburger, G.: Verdichtung von Echolot-Querprofilen unter Berücksichtigung der Flussmorphologie, Österr. Z. Vermessung & Geoinformation, 4, 211–214, 2000. 3619

Mandlburger, G.: Topographische Modelle für Anwendungen in Hydraulik und Hydrologie, Ph.D. thesis, Vienna University of Technology, 2006. 3614, 3616

Marco, J. B.: Flood risk mapping, Kluwer Academic Publishers, Dordrecht, 353–373, 1994. 3607

Menendez, M.: Design discharge calculations and flood plain management, European Comission (Directorate, General XII), Cemagref, 53–82, 2000. 3607

Nardinocchi, C., Forlani, G., and Zingaretti, P.: Classification and Filtering of Laser Data, in: International Archives of Photogrammetry and Remote Sensing, XXXIV, 3/W13, Dresden, Germany, 2003. 3612

Nujic, M.: Praktischer Einsatz eines hochgenauen Verfahrens für die Berechnung von tiefengemittelten Strömungen, Ph.D. thesis, Universität der Bundeswehr München, Institut für Wasserwesen, Prof. W. Bechteler (superv.), Mitteilungen Nr. 62, 1999. 3608, 3616

Petraschek, A.: Risk assessment and hazard zone planning in Switzerland, Österr. Wasser- und Abfallwirtschaft, 54, 123–127, 2002. 3607

Pfeifer, N. and Mandlburger, G.: Topographic Laser Ranging and Scanning: Principles and Processing, chap. Filtering and DTM Generation, CRC Press, 2008. 3611

Pfeifer, N., Stadler, P., and Briese, C.: Derivation of Digital Terrain Models in the SCOP++ Environment, in: Proceedings of OEEPE Workshop on Airborne Laserscanning and Interferometric SAR for Detailed Digital Terrain Models, Stockholm, Sweden, 2001. 3612

Pironneau, P.: Finite Element Methods for Fluids, Masson, Paris, 1989. 3617

Rabus, B., Eineder, M., Roth, A., and Bamler, R.: The shuttle radar topography missiona new class of digital elevation models acquired by spaceborne radar, ISPRS J. Photogramm. Rem. S., 57, 241–262, 2003. 3610

RIWA-T: Technische Richtlinien für die Bundeswasserbauverwaltung, Bundesministerium für

Land- und Forstwirtschaft, Umwelt und Wasserwirtschaft, 2006. 3607, 3618

Schenk, T.: Modeling and recovering systematic errors in airborne laser scanners, in: Proceedings of OEEPE Workshop on Airborne Laserscanning and Interferometric SAR for Detailed Digital Terrain Models, Stockholm, Sweden, 2001. 3614

5   SCOP++: Institute of Photogrammetry and Remote Sensing, www.ipf.tuwien.ac.at/products/products.html, 2008. 3618

Sinha, S., Sotiropoulus, F., and Odgaard, A.: Three-dimensional numerical model for flow through natural rivers, J. Hydraulic Eng., 124, 14–24, 1998. 3608

Sithole, G. and Vosselman, G.: Experimental comparison of filtering algorithms for bare-earth
10   extraction from airborne laser scanning point clouds, ISPRS J. Photogramm. Rem. S., 59, 85–101, 2004. 3612

Sithole, G. and Vosselman, G.: Filtering of airborne laser scanner data based on segmented point clouds, in: International Archives of Photogrammetry and Remote Sensing, XXXVI, 3/W19, 66–71, Enschede, The Netherlands, 2005. 3612

15   Sohn, G. and Dowman, I.: Terrain surface reconstruction by the use of tetrahedron model with the MDL Criterion, in: International Archives of Photogrammetry and Remote Sensing, XXXIV, 3B, 336–344, Graz, Austria, 2002. 3611

TopoSys: Topographische Systemdaten GmbH, http://www.toposys.de/, 2008. 3610

Tóvari, D. and Pfeifer, N.: Segmentation based robust interpolation – a new approach to laser
20   data filtering, in: International Archives of Photogrammetry and Remote Sensing, XXXVI, 3/W19, pp. 79–84, Enschede, The Netherlands, 2005. 3612

von Hansen, W. and Vögtle, T.: Extraktion der Geländeoberfläche aus flugzeuggetragenen Laserscanner-Aufnahmen, Photogrammetrie Fernerkundung Geoinformation, 4, 229–236, 1999. 3611

25   Vosselman, G.: Slope based filtering of laser altimetry data, in: International Archives of Photogrammetry and Remote Sensing, XXXIII, B3, 935–942, Amsterdam, Netherlands, 2000. 3611

Wagner, W., Ullrich, A., Melzer, T., Briese, C., and Kraus, K.: From single-pulse to full-waveform airborne laser scanners: potential and practical challenges, in: International Archives of
30   Photogrammetry and Remote Sensing, XXXV, Istanbul, Turkey, 2004. 3612

Watt, W.: Twenty Years of Flood Risk Mapping Under Canadian National Damage Reduction Program, Kluwer Academic Publishers, Dordrecht, 155–165, 2000. 3607

Optimisation of LiDAR DTMs for river flow modelling

G. Mandlburger et al.

Title Page

Abstract	Introduction
Conclusions	References
Tables	Figures

|◄ | ►|

◄ | ►

Back | Close

Full Screen / Esc

Printer-friendly Version

Interactive Discussion

Zhang, K., Chen, S.-C., Whitman, D., Yan, J., and Zhang, C.: A progressive morphological filter for removing nonground measurements from airborne LIDAR data, IEEE T. Geosci. Remote,, 41, 872–882, 2003. 3611

Optimisation of LiDAR DTMs for river flow modelling

G. Mandlburger et al.
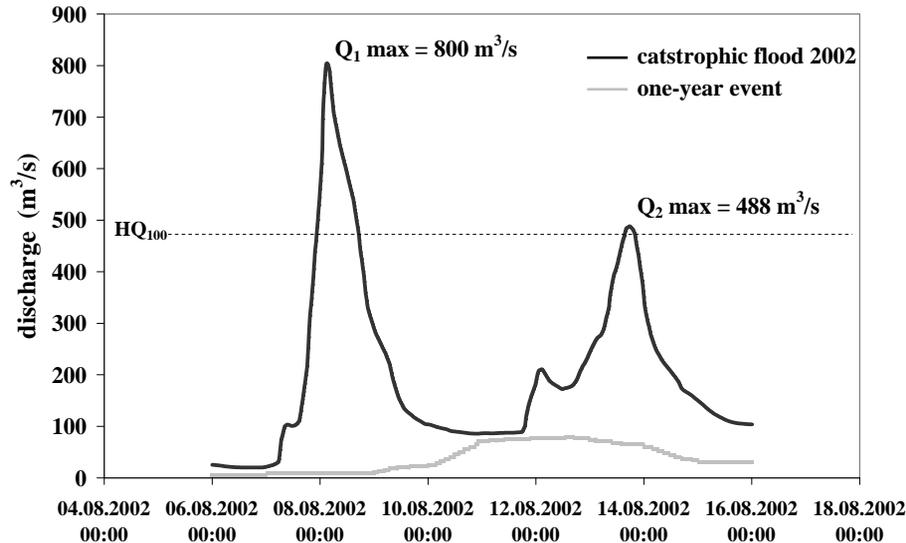
Fig. 1. Hydrograph recorded at gauging station Stiefern during the catatstrophic flood in August 2002 (6–16 August) featuring two peaks (800 m^3/s on Aug 8; 488 m^3/s on Aug 15) (black line); hydrograph of a one-year flood at gauging station Stiefern (grey line); the hydrographs are compared to the discharge of a 100-year flood (Q=470 m^3/s, black dashed line).
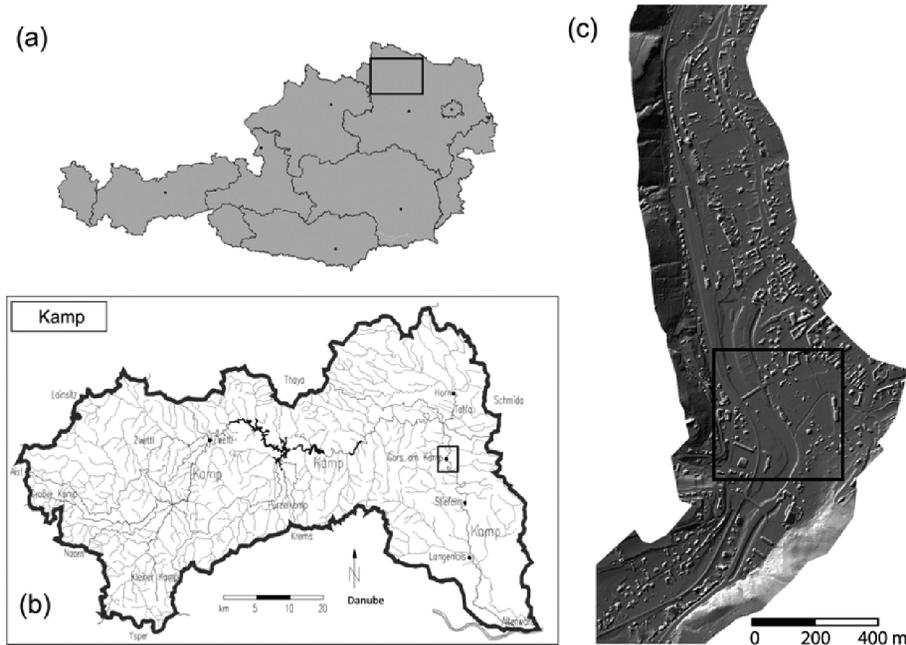
Fig. 2. (a) Map of Austria including the river Kamp system; **(b)** catchment area of the river Kamp with main tributaries (E 15°26′, N 48°32′; extension: 47 km×23 km); **(c)** River section (Gars am Kamp), shaded relief map of the Digital Surface Model.
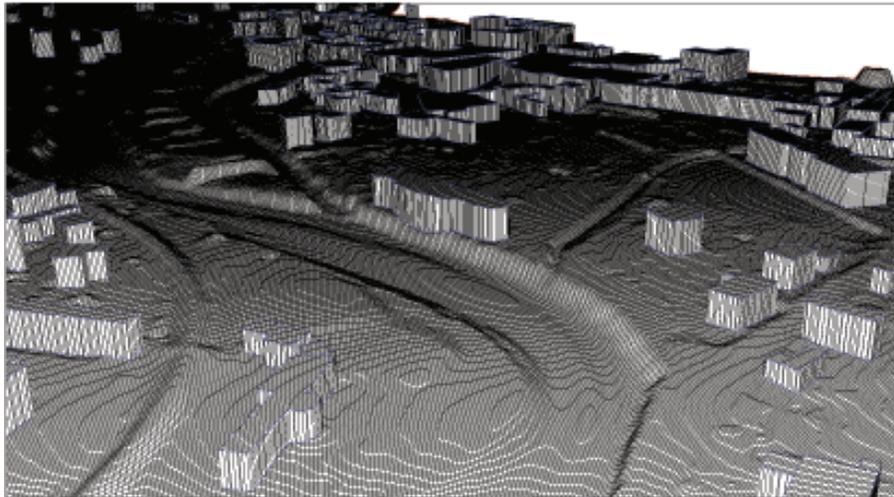
Fig. 3. Perspecitve view of the final 1 m DTM-W of Gars am Kamp including the Dungl hotel (image center), buildings are considered as block models and integrated as breaklines into the hybrid grid.

Title Page

Abstract   Introduction

Conclusions   References

Tables   Figures

◄◄   ►►

◄   ►

Back   Close

Full Screen / Esc

Printer-friendly Version

Interactive Discussion
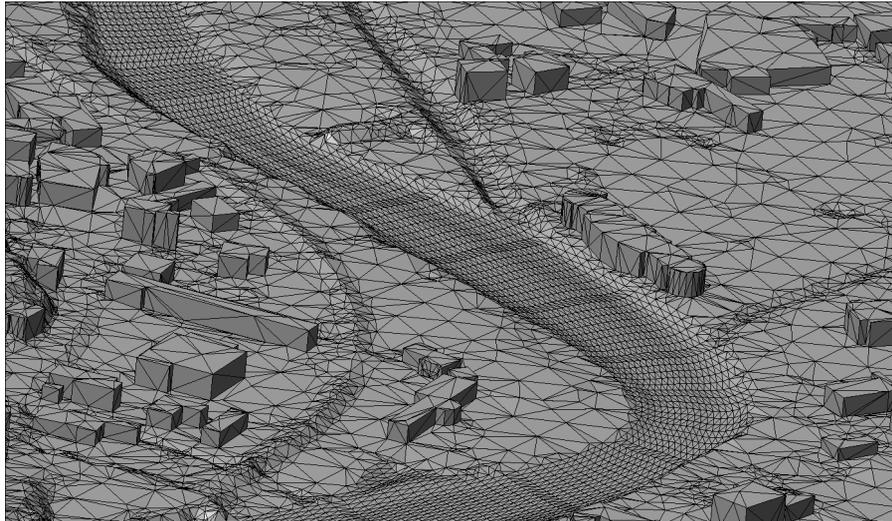
Fig. 4. Perspective view of a professionally thinned and conditioned DTM-W TIN, which also serves as hybrid hydraulic computation mesh (c.f. geometry (b)); overbank area: irregular distribution of mesh nodes (i.e. unstructured grid), river bed and river bank: cells aligned to the principal flow direction (i.e. structured grid).

G. Mandlburger et al.

(a)   *(b)*
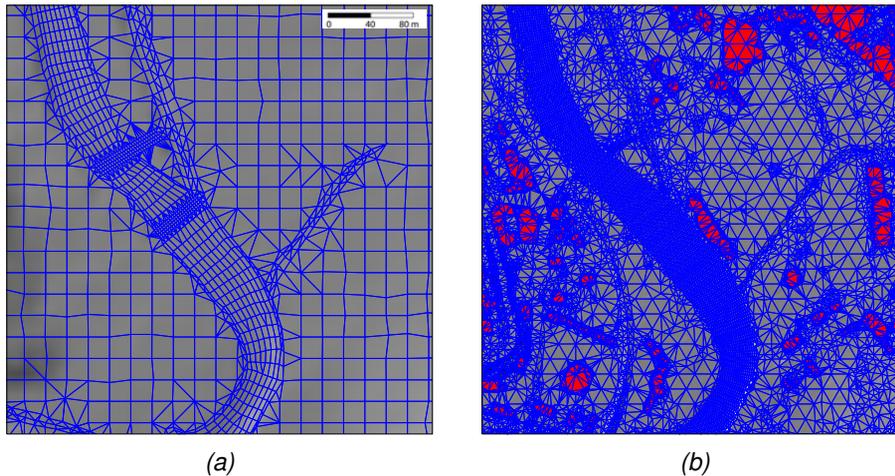
Fig. 5. Computation grid of two geometry variants (a) and (b) for HN modelling, Gars/Kamp, Lower Austria; **(a)** Regular $20{\times}20\,\text{m}^2$ grid, additional breaklines for description of river bank and weir channel, river bed: structured grid; **(b)** Hybrid grid derived from 1 m LiDAR DTM-W via adaptive TIN refinement and subsequent mesh conditioning, river bed and river bank: structured grid (post spacing 5 m in / 2 m perpendicular to flow direction), over bank area: unstructured grid: maximum height tolerance $\Delta z_{\text{max}}{=}{\pm}20\,\text{cm}$, buildings in red.
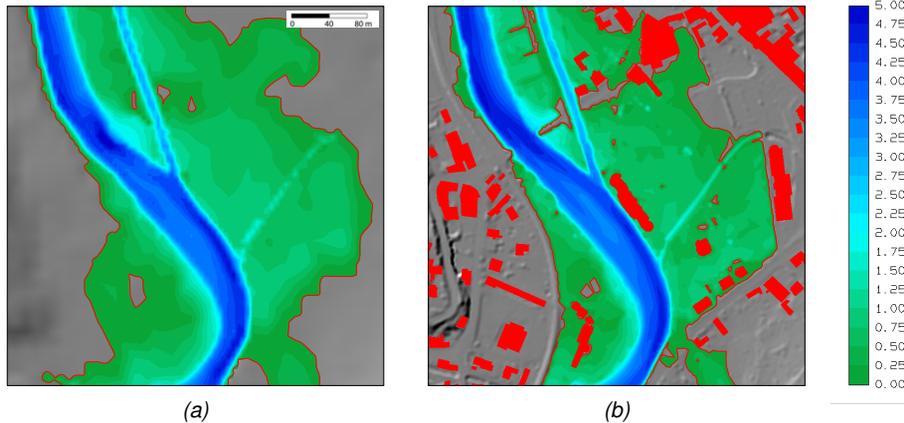
Fig. 6. Flood extents (red boundary line) and water depths [m] for a simulated HQ100 (470 m^3/s) in Gars/Kamp; **(a)** extended flooding of residential area beyond the dams; **(b)** inundation area restricted by dams (e.g. railway dam).

(a) *(b)*
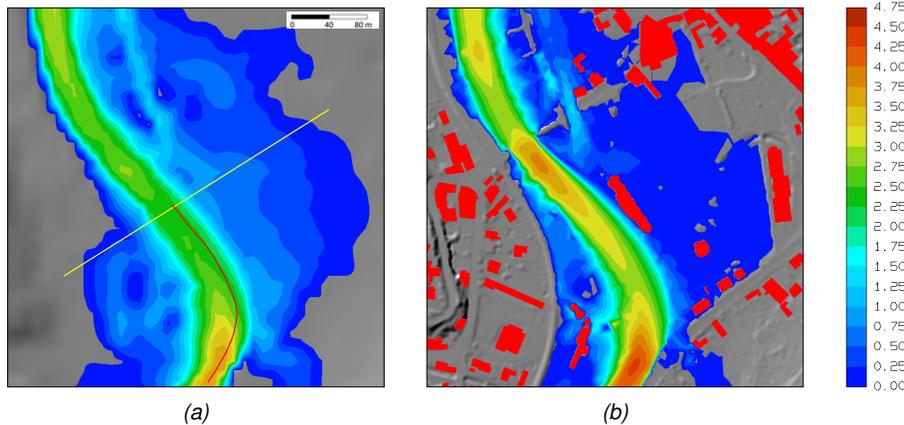
Fig. 7. Flow velocities [m/s] for a simulated HQ100 (470 m^3/s) in Gars/Kamp; **(b)** shows higher flow velocities in the main channel compared to **(a)**, floodplain: higher velocities in (a) than in (b).

Optimisation of LiDAR DTMs for river flow modelling

G. Mandlburger et al.
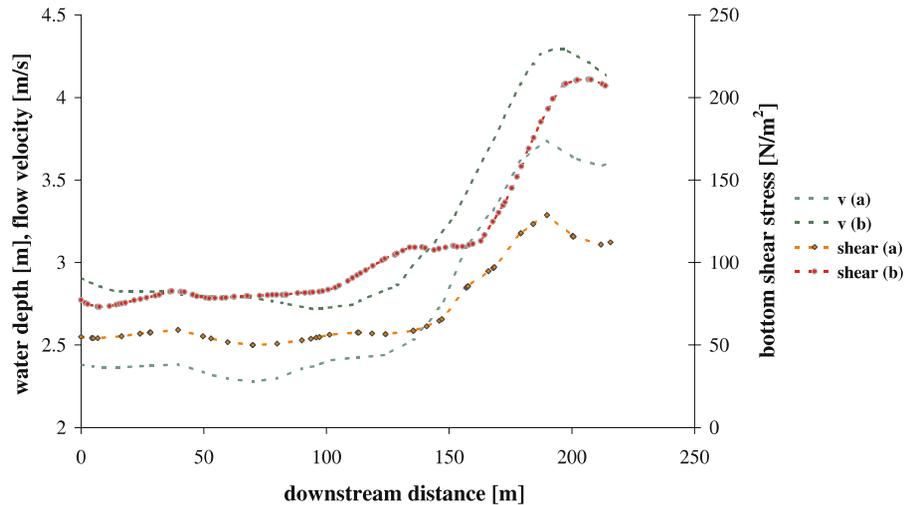
Fig. 8. Flow velocity [m/s] and bottom shear stress [N/m^2] of a longitudinal section for a simulated HQ100 (470 m^3/s) in Gars/Kamp.

Full Screen / Esc
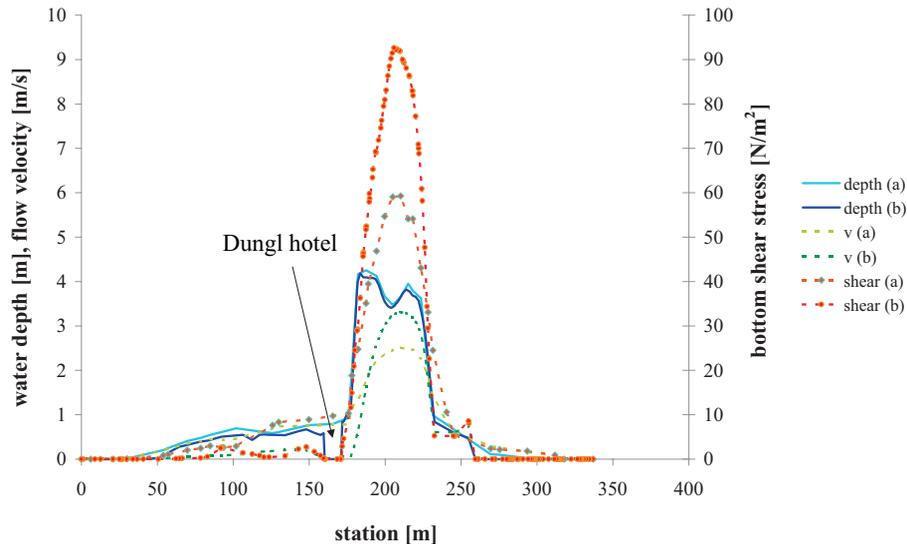
Fig. 9. Water depth [m], flow velocity [m/s] and bottom shear stress [N/m^2] of a cross section including the Dungl hotel following the left river bank for a simulated HQ100 (470 m^3/s) in Gars/Kamp.